





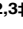


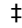
SHORT REPORTS

Seipin traps triacylglycerols to facilitate their nanoscale clustering in the endoplasmic reticulum membrane

Xavier Prasanna¹ , Veijo T. Salo^{2,3} , Shiqian Li^{2,3} , Katharina Ven^{2,3},
Helena Vihinen⁴ , Eija Jokitalo⁴ , Ilpo Vattulainen^{1‡} , Elina Ikonen^{2,3‡*} 

1 Department of Physics, University of Helsinki, Helsinki, Finland, **2** Department of Anatomy, Faculty of Medicine, University of Helsinki, Helsinki, Finland, **3** Minerva Foundation Institute for Medical Research, Helsinki, Finland, **4** Institute of Biotechnology, University of Helsinki, Helsinki, Finland

 These authors contributed equally to this work.

 These authors are joint senior authors on this work.

* elina.ikonen@helsinki.fi



OPEN ACCESS

Citation: Prasanna X, Salo VT, Li S, Ven K, Vihinen H, Jokitalo E, et al. (2021) Seipin traps triacylglycerols to facilitate their nanoscale clustering in the endoplasmic reticulum membrane. *PLoS Biol* 19(1): e3000998. <https://doi.org/10.1371/journal.pbio.3000998>

Academic Editor: Ana J. Garcia-Saez, Universitat zu Koln, GERMANY

Received: March 3, 2020

Accepted: November 2, 2020

Published: January 22, 2021

Copyright: © 2021 Prasanna et al. This is an open access article distributed under the terms of the [Creative Commons Attribution License](https://creativecommons.org/licenses/by/4.0/), which permits unrestricted use, distribution, and reproduction in any medium, provided the original author and source are credited.

Data Availability Statement: All relevant data are within the paper and its [Supporting Information](#) files. Input files for simulations are available from Zenodo (DOI: [10.5281/zenodo.3907015](https://doi.org/10.5281/zenodo.3907015)).

Funding: This study was financially supported by the Academy of Finland (<https://www.aka.fi/en>) Center of Excellence Program (grant 307415 to EI and IV), Academy of Finland grants (282192 and 312491 to EI; 287975 to EJ), Sigrid Juselius Foundation (EI, IV), Jane and Aatos Erkko Foundation (<http://jaes.fi/en/>) (EI) and the HiLIFE

Abstract

Seipin is a disk-like oligomeric endoplasmic reticulum (ER) protein important for lipid droplet (LD) biogenesis and triacylglycerol (TAG) delivery to growing LDs. Here we show through biomolecular simulations bridged to experiments that seipin can trap TAGs in the ER bilayer via the luminal hydrophobic helices of the protomers delineating the inner opening of the seipin disk. This promotes the nanoscale sequestration of TAGs at a concentration that by itself is insufficient to induce TAG clustering in a lipid membrane. We identify Ser166 in the $\alpha 3$ helix as a favored TAG occupancy site and show that mutating it compromises the ability of seipin complexes to sequester TAG in silico and to promote TAG transfer to LDs in cells. While the S166D-seipin mutant colocalizes poorly with promethin, the association of nascent wild-type seipin complexes with promethin is promoted by TAGs. Together, these results suggest that seipin traps TAGs via its luminal hydrophobic helices, serving as a catalyst for seeding the TAG cluster from dissolved monomers inside the seipin ring, thereby generating a favorable promethin binding interface.

Introduction

Lipid droplets (LDs) are intracellular storage organelles critical for energy metabolism [1,2]. LDs consist of neutral lipids, mainly triglycerides (triacylglycerols [TAGs]) and sterol esters, surrounded by a phospholipid (PL) monolayer. LD biogenesis takes place in the endoplasmic reticulum (ER), where DGAT enzyme activity induces TAG deposition in the bilayer [3–5]. However, PL bilayers can only accommodate a low concentration (circa 3 mole percent [mol%]) of TAGs before TAGs tend to phase separate. With rising local TAG concentration in the membrane, TAGs are thought to cluster and form nanometer-sized lens-like structures [6] that then bud out to the cytoplasmic side of the ER [7,8]. The formed LDs retain a functional connectivity with the ER via membranous bridges that allow their further growth [9,10].

Fellow Program (<https://www.helsinki.fi/en/helsinki-institute-of-life-science>) (EI, IV, EJ); VS acknowledges support from the Doctoral Programme in Biomedicine (<https://www.helsinki.fi/en/research/doctoral-education/doctoral-schools-and-programmes/doctoral-school-in-health-sciences/doctoral-programme-in-biomedicine>), Finnish Medical Foundation (<https://laaketieteensaatio.fi/en/home/>), Paulo Foundation (<https://www.paulo.fi/in-english>), Alfred Kordelin Foundation (<https://kordelin.fi/en/frontpage>), Maud Kuistila Foundation (<https://mkmsaatio.fi/en/the-maud-kuistila-memorial-foundation/>), Biomedicum Helsinki Foundation (<http://www.biomedicum.fi/index.php?page=112&lang=2>) and Emil Aaltonen Foundation (<https://emilaaltonen.fi/apurahat/in-english/>). The funders had no role in study design, data collection and analysis, decision to publish, or preparation of the manuscript.

Competing interests: The authors have declared that no competing interests exist.

In silico work complementing experiments has turned out to be instrumental in deciphering nanoscale cellular processes [11,12]. In simulations, TAGs form lens-like lipid clusters inside a lipid bilayer, giving rise to blister-like membrane regions [13]. Their emergence from the ER can be modulated by ER topology, membrane asymmetry, surface tension, and PL composition [14–19]. Moreover, the process by which the membrane properties of the TAG-engulfed LD monolayer regulate protein recruitment to LDs is starting to emerge [20–22]. However, it is not known if the initial process of TAG clustering in the ER is modulated by proteins.

The ER protein seipin is critical for LD assembly and adipogenesis [23–26], and its mutations result in lipodystrophies or neuronal disorders [27–30]. In the ER, seipin forms disk-like oligomers consisting of 11 subunits in human cells [31]. Based on cryo-electron microscopy (cryo-EM) structures of the seipin luminal regions, each protomer contains a lipid binding domain and a hydrophobic, membrane-anchored helix [31,32]. Indeed, seipin has been proposed to control cellular PL metabolism, especially phosphatidic acid handling [33], and/or to play a structural role at LDs forming subdomains and ER–LD contacts [34–38].

Seipin can determine where LDs form [35]. Without seipin, LDs appear to spontaneously “oil out” of the ER in the form of tiny and supersized LDs [34,39,40]. Seipin interacts with promethin, a multi-transmembrane protein with homology to ER-shaping reticulon proteins [41–43], and this interaction is somehow important during early LD assembly [44]. Upon LD growth, promethin disassembles from seipin and decorates the surface of LDs, whilst seipin remains at the ER–LD neck. We recently reported that seipin facilitates TAG delivery to the LD and counteracts ripening-induced shrinkage of small LDs [35]. How this seipin-mediated TAG flux may be achieved is not known. Here, we address this question by combining biomolecular simulations and cell-based experiments. Our results suggest that the seipin complex, via its hydrophobic membrane intercalated helices, can trap TAGs in the bilayer, thereby serving as a seed for TAG clustering inside the lumen of the seipin ring. This appears to generate a favorable interface for promethin binding and constitutes a critical step for further LD growth.

Results/Discussion

TAG clusters in the lumen of the seipin oligomer

To investigate the role of seipin in regulating TAG distribution, we conducted molecular dynamics (MD) simulations. We constructed a model of the seipin oligomer based on the cryo-EM structure of the luminal domains of human seipin [31] and modeled the transmembrane domains (TMDs) on the structure based on their amino acid sequence. The resulting model was placed in a multi-component bilayer, whose lipid composition mimics that of the ER (S1A Fig; S1 Table).

An initial trigger for LD biogenesis is the generation of TAGs within the ER. We thus placed free TAG molecules (2.5 mol%) within the model bilayer with or without the seipin oligomer, and carried out coarse-grained simulations for up to 30 μ s. In both systems, TAGs rapidly clustered to form lens-like structures (Fig 1A and 1B), in line with previous in vitro and in silico work, indicating limited solubility of TAG in PL bilayers [13,45]. Remarkably, in the presence of seipin, TAG clustering occurred invariably within the lumen of the disk-shaped seipin oligomer (Fig 1B).

We next mapped the TAG occupancy of seipin amino acid residues by analyzing the probability of each residue to be in close proximity to a TAG molecule. The TMDs showed affinity for TAG, but the highest TAG occupancy, especially at later simulation times, was observed for 3 residues in the hydrophobic, membrane-anchored α 2– α 3 helix of seipin, namely V163, F164, and S166 (Fig 1C and 1D). These data suggest that TAGs cluster in the lumen of the

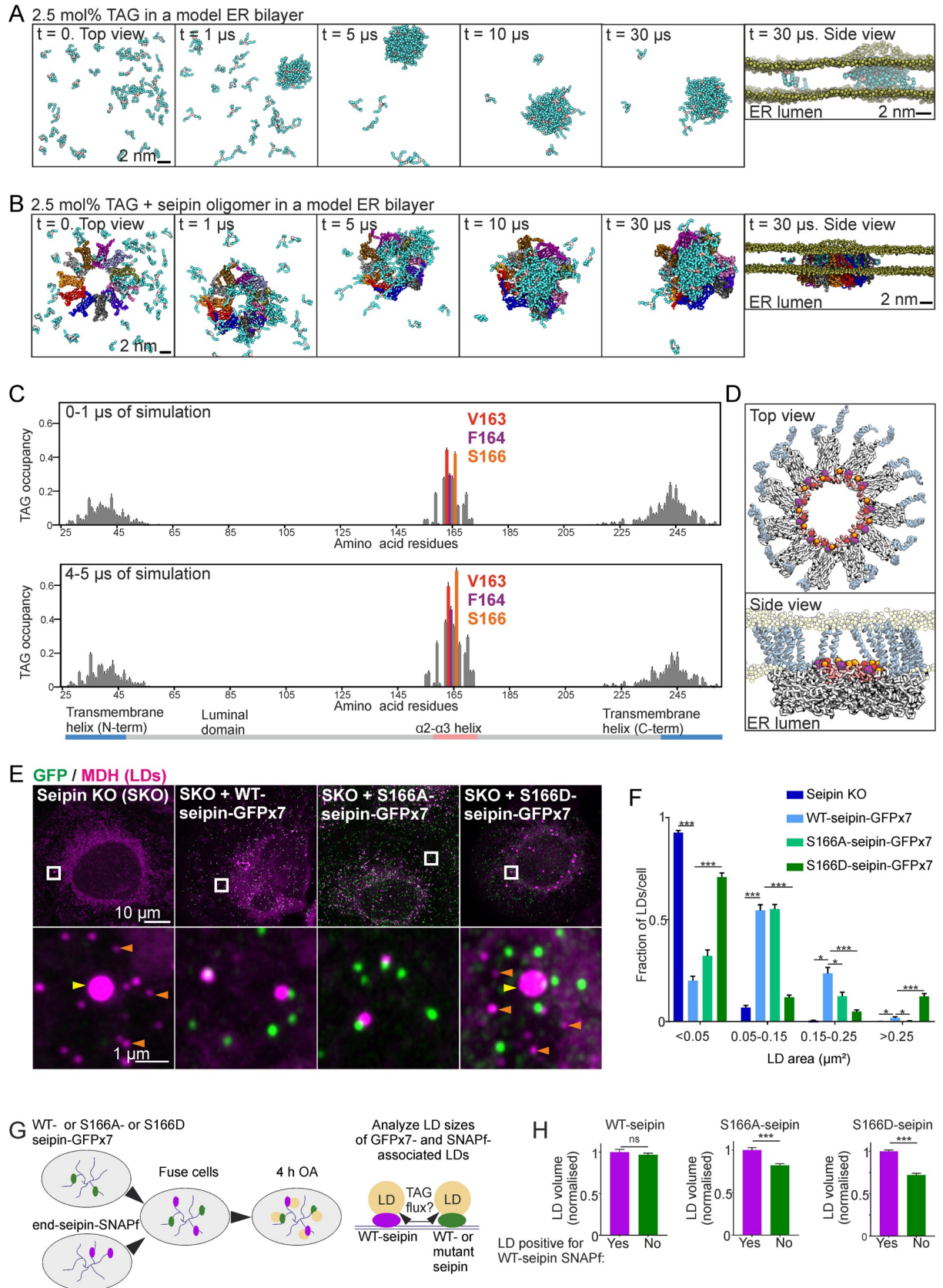


Fig 1. The luminal hydrophobic helix is important for TAG clustering within the seipin disk. (A) Snapshots of coarse-grained simulations in the absence of seipin with 2.5 mol% TAG in an ER bilayer. For clarity, PL head groups (yellow) are only shown in the side view, and water is not shown. The acyl chains of TAGs are shown in cyan; glycerol moiety is in light brown. (B) Snapshots of simulations as in (A), but in the presence of seipin. (C) TAG occupancy data of simulations demonstrated in (B). TAG occupancy for each amino acid residue is defined as the probability that the residue has a TAG molecule within 0.5 nm distance from its surface. The TAG occupancies for the initial (0–1 μ s) and later (4–5 μ s) stages of the simulation are plotted separately. Bars: mean \pm SEM, $n = 10$ replicates. (D) Key residues from (C) are highlighted. (E) A431 SKO cells stably expressing indicated plasmids were delipidated for 3 d and treated with 200 μ M OA for 1 h. Cells were fixed, LDs stained, and cells imaged by Airyscan microscopy. Maximum intensity projections of z -stacks. Orange arrowheads: tiny LDs; yellow arrowheads: supersized LDs. (F) Analysis of (E). Bars: mean \pm SEM, $n \geq 60$ cells/group, 3–4 experiments. Statistics: Kruskal–Wallis test followed by Dunn’s test, comparing against WT-seipin-GFPx7. (G) End-seipin-SNAPf cells and SKO cells stably expressing WT-, S166A-, or S166D-seipin-GFPx7 were co-plated for 2 d in delipidation conditions. Cells were fused with polyethylene glycol, and 12–14 h later 200 μ M OA and SNAP-Cell 647-SiR were added to the cells. Four hours after this, LDs were stained with MDH, and fused cells were imaged live. (H) Analysis of (G). The sizes of end-seipin-SNAPf-associated LDs were compared to LDs within the same cell not positive for SNAPf. Bars: mean \pm SEM, $n = 152$ –659 LDs/group, 4–20 fused cells/group, 2 experiments. Statistics: Mann–Whitney test. Exemplary micrographs are shown in [S1D Fig](#). Numerical values for the graphs in (C), (F), and (H) can be found in [S1 Data](#). ER, endoplasmic reticulum; KO, knockout; LD, lipid droplet; MDH, monodansylpentane; mol%, mole percent; OA, oleic acid; SKO, seipin knockout; TAG, triacylglycerol; WT, wild-type.

<https://doi.org/10.1371/journal.pbio.3000998.g001>

seipin oligomer and that distinct residues of the hydrophobic helices delineating the inner opening of the seipin ring play an important role in this.

S166 is critical for seipin function

To assess the relevance of the residues identified as preferential TAG interaction sites, we analyzed whether mutating them would affect seipin function in LD biogenesis. We designed a panel of single amino acid substitution mutants, tagged them with split GFPx7 [46], and expressed them in human A431 seipin knockout (SKO) cells. We used fluorescence-activated cell sorting (FACS) to enrich stable pools with near-endogenous seipin expression levels. Cells were then delipidated, treated with oleic acid (OA) to induce LD biogenesis, and imaged by Airyscan microscopy. In cells without detectable GFP (i.e., SKO cells), LDs were tiny or supersized, as expected ([Fig 1E and 1F](#)). Expression of WT-seipin-GFPx7 rescued this phenotype, with single seipin foci associated with virtually all LDs ([Figs 1E, 1F and S1B](#)), as previously reported [34]. Mutations affecting V163 or F164 led to a more diffuse reticular GFP fluorescence pattern compared to WT-seipin, suggesting they may affect seipin complex assembly ([S1B Fig](#)). However, single seipin foci could also still be discerned, and these were often juxtaposed with LDs, and the LD morphology was similar to that of the WT-seipin-GFPx7-expressing cells ([S1B Fig](#)). The notion that the oligomerization propensity of seipin may be sensitive to mutations in V163 and F164 is in line with the fact that these residues reside at the seipin protomer–protomer interface [31].

In contrast to mutations affecting V163 and F164, mutation of S166 did not appear to impair seipin complex formation, as the mutants tested existed as discrete puncta in cells ([S1B Fig](#)). S166A-seipin rescued the overall LD morphology in SKO cells, but LDs were on average somewhat smaller than in WT-seipin-expressing cells ([Figs 1E, 1F, S1B and S1C](#)). Importantly, S166D-seipin was not able to complement the LD biogenesis defect in SKO cells, as most cells contained supersized and tiny LDs ([Figs 1E, 1F, S1B and S1C](#)).

We previously reported that seipin can promote the growth of its associated LD: In a continuous ER with both seipin-containing LDs and LDs where seipin had been acutely depleted, seipin-containing LDs grew at the expense of seipin-depleted ones [35]. To study whether the S166-mutants can promote the growth of existing LDs as well as WT-seipin, we performed competition experiments employing heterologous cell fusions ([Fig 1G](#)). In a continuous ER network with LDs associated with either S166-mutant or WT-seipin, the growth of S166D- or S166A-seipin-associated LDs was reduced compared to WT-seipin-associated LDs, suggesting that the S166-mutants are defective in promoting LD growth ([Figs 1G, 1H and S1D](#)).

Altogether, these data imply that mutating S166 to Asp impairs seipin function both in initial LD assembly and subsequent LD growth, whilst mutating S166 to Ala affects the growth of assembled LDs.

Having identified a key seipin residue for TAG interaction, we performed atomistic MD simulations of the situation where TAGs are clustered within the seipin disk. These revealed that S166 tends to form a complex with TAG (Fig 2A and 2B). Simultaneous interaction was observed between a TAG molecule and S166 as well as the neighboring S165 (Fig 2B). The interaction involved formation of a hydrogen bond between a carbonyl group of the TAG molecule and the amino acid backbone of S166. This interaction appeared to be further stabilized by formation of a transient hydrogen bond between another carbonyl group of the same TAG molecule and the side chain of S165, reducing the diffusion of the associated TAG. By calculating the short-time (nanosecond scale) diffusion coefficient D , we observed that the D of TAGs not interacting with S166 (magenta trajectory in Fig 2A) was approximately 3 times larger than the D of TAG bound to S166 (red trajectory in Fig 2A).

To simulate S166-mutants in this context, we changed all S166 residues to either Asp or Ala after the formation of a stable S166–TAG complex. The simulations revealed that interaction of TAG with S166D was significantly weaker than with S166, whilst switching to S166A did not similarly impair the interaction. The short-time diffusion coefficient of TAG bound to S166D was approximately 50% larger than that of TAG bound to S166 (Fig 2A). The S166D–TAG complexes were also less stable, with a lifetime of approximately 0.1 μ s compared to approximately 0.5 μ s for S166–TAG and S166A–TAG complexes. The short-time diffusion coefficient of TAG bound to S166A was approximately 15% larger than that of TAG bound to S166. Finally, as the 165A/166A double mutant has been reported to impair seipin function [44], we switched both S165 and S166 to Ala and found that this switch also impaired TAG–S166 interaction, with the short-time diffusion coefficient of TAG being approximately 100% larger than the D of TAG bound to S166, and a lifetime of approximately 0.1 μ s for the S166A–TAG complex.

In summary, these data suggest that S166 serves as a nucleation site in the formation of TAG clusters. Given that there are 11 S166 residues in the seipin complex, it seems evident that the TAG clusters forming around S166 residues gradually merge and promote the growth of a larger cluster.

S166D-seipin overexpression induces ER membrane deformation

We next assessed the effects of the S166D change on the neighboring PLs in simulations with or without a TAG cluster in the seipin disk. There was no significant movement of the α 2– α 3 helices towards the core of the bilayer in either condition in WT- or S166D-seipin-containing systems (S2A–S2D Fig). However, the bilayer was locally deformed in the presence of S166D-seipin, with apparent bulging of the PL head groups towards the membrane interior on both bilayer leaflets (Fig 2C). In line with this, topological maps of the leaflets displayed higher negative and positive curvatures in simulations with S166D-seipin compared to WT-seipin (Fig 2D). These effects were apparently related to the negative charge of Asp, as protonation of S166D in the simulations alleviated the membrane perturbation (S2E and S2F Fig).

In cells stably expressing S166D-seipin, the mutant protein was present as typical seipin puncta (Fig 1E). However, higher transient overexpression of S166D-seipin induced a gradual, dramatic reorganization of the ER into membranous aggregates, whilst high expression of WT-seipin did not induce this (Figs 2E and S2G). Electron microscopy analysis revealed that these aggregates consisted of small ER sacs connected by membranous constrictions (Fig 2F–2H). Intriguingly, these constrictions were approximately 15 nm in diameter, similar to the

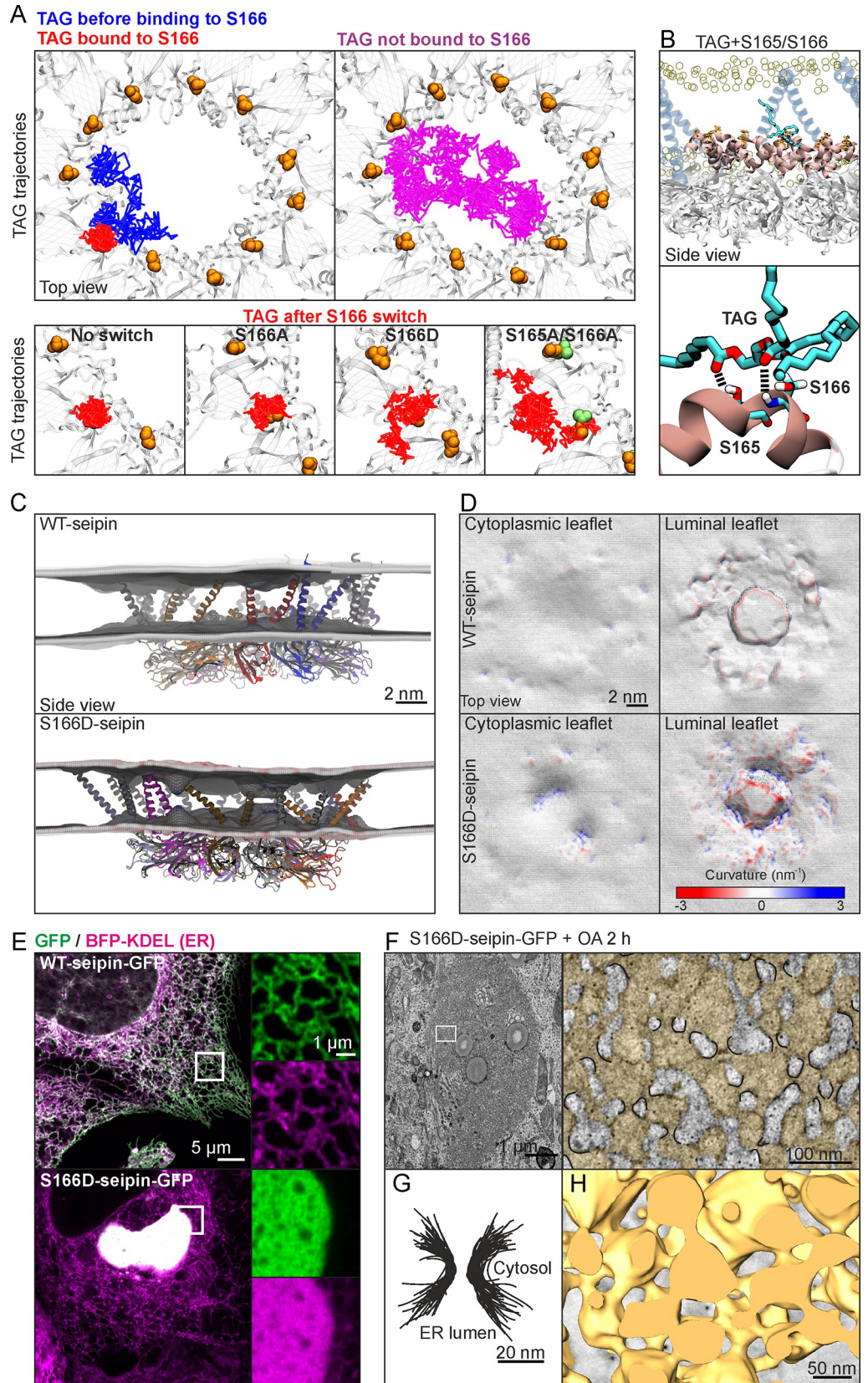


Fig 2. S166D-seipin impairs TAG interaction and induces ER membrane deformation. (A) Exemplary TAG trajectories from an atomistic simulation with a TAG cluster within the seipin disk. Blue indicates TAG trajectory prior to S166 binding (0–590 ns), red shows its trajectory upon S166 binding (591–960 ns). Magenta indicates the trajectory of TAG not interacting with S166 (0–960 ns). Lower row, left: higher magnification of S166-binding TAG trajectory. Lower row, other insets: TAG trajectories after indicated amino acid changes (trajectory lengths are 370 ns for all insets). Each line represents a series of in-plane 1-ns displacements. (B) Snapshot of the interface between a TAG molecule and S165 and S166. Hydrogen bonds between the carbonyl groups of the TAG molecule and S165 and S166 are represented by black dashed parallel lines. The α 2– α 3 helix is shown in beige. (C) Snapshots of atomistic simulations of WT- or S166-seipin, performed with 2.5 mol% TAG in the membrane. The time-averaged ($>1 \mu$ s) mean curvature of bilayer leaflets from the plane of phospholipid head groups is shown. (D) Topologies and the mean curvature of the bilayer leaflets from (C) are shown. (E) A431 cells stably expressing BFP-KDEL were transfected with WT- or S166D-seipin-GFP for 3 d and imaged live by Airyscan microscopy. (F) HEK293A cells were transfected with S166D-seipin-GFP for 3 d in delipidation conditions and treated with 200 μ M OA for 2 h. Transmission electron microscopy images of the membranous aggregates display periodical ER constrictions (indicated with black in the zoom-in; ER is colored with yellow). (G) Segmented membrane constrictions from (F) are overlaid. (H) Cells were treated as in (F) and imaged by electron tomography. A 3D model of the ER sacs (yellow) induced by S166D-seipin-GFP is shown. ER, endoplasmic reticulum; mol%, mole percent; OA, oleic acid; TAG, triacylglycerol; WT, wild-type.

<https://doi.org/10.1371/journal.pbio.3000998.g002>

seipin oligomer disk. It is tempting to speculate that the bilayer destabilization observed with Asp in simulations may contribute to these ER membrane deformations, although the protonation status of S166D in cells remains open.

S166D-seipin shows reduced colocalization with promethin

The interaction of promethin and seipin requires the luminal hydrophobic helix of seipin [44], which also harbors the amino acids identified in our simulations as maximal TAG occupancy sites. We thus reasoned that the S166-mutants may impact seipin–promethin interaction. To investigate this, we performed immunofluorescence staining using anti-promethin antibodies. These reliably detected endogenous promethin, as evidenced by using CRISPR/Cas9-engineered promethin KO cells as controls (S3A and S3B Fig). Furthermore, in line with previous reports [41,44], the antibodies demonstrated that promethin levels increased upon prolonged OA incubation, and this was accompanied by relocalization of promethin to rings around LDs (S3C–S3E Fig). In cells grown in complete medium, we found promethin as discrete dots, many of which overlapped with WT-seipin dots (Fig 3A and 3B). Indeed, approximately 60% of WT-seipin foci were positive for promethin, and similar results were found for S166A-seipin (Figs 3A, 3B and S3F). In contrast, only a small fraction (approximately 10%) of S166D-seipin overlapped with promethin, indicating that S166D impairs seipin association with promethin (Figs 3A, 3B and S3F).

Promethin depletion sensitizes cells to rapid seipin removal

To further investigate the interplay between seipin and promethin, we generated promethin KO cell pools on top of seipin degron cells, where seipin can be rapidly depleted using the auxin-inducible degron (AID) system [35,47,48]. Promethin depletion did not interfere with the AID system, as seipin was efficiently depleted in both control and promethin KO cells upon addition of indole-3-acetic acid (IAA) (S3G and S3H Fig). Upon promethin KO, seipin levels increased (S3G and S3H Fig) and LDs were fewer in number but larger in size (S3I Fig), as reported [44].

This system allowed us to scrutinize the effects of rapid seipin removal on LD biogenesis in the presence versus absence of promethin. We have previously noted that upon acute seipin degradation (from promethin-containing cells), the characteristic phenotype of numerous tiny and a few supersized LDs only appears after a refractory period [35]. Thus, removing seipin only 30 min prior to LD induction is not sufficient to evoke the SKO phenotype, while it

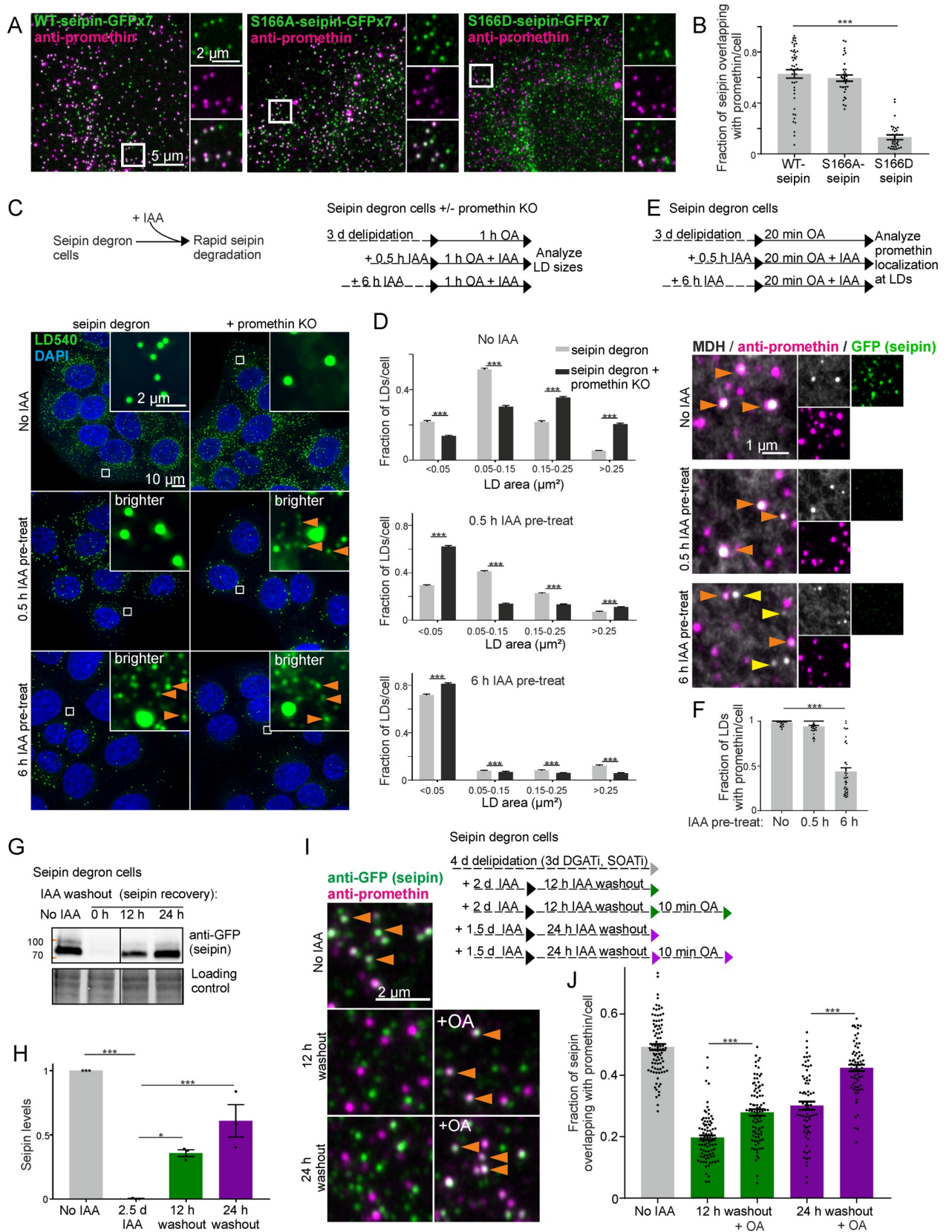


Fig 3. Promethin sensitizes cells to seipin depletion, and TAG facilitates nascent seipin association with promethin. (A) A431 seipin KO cells stably expressing indicated plasmids were fixed and stained with anti-promethin antibodies. (B) Analysis of (A). Bars: mean \pm SEM, $n \geq 30$ cells/group, 3–4 experiments. Statistics: Kruskal–Wallis test followed by Dunn’s test, comparing to WT-seipin. (C) Seipin degron cells with or without promethin KO were delipidated for 3 d, treated with IAA and 200 μ M OA as indicated, fixed, stained, and imaged by widefield microscopy. Deconvolved maximum intensity projections of z-stacks. Orange arrowheads: tiny LDs. Note that 0.5-h IAA pretreatment is sufficient to induce generation of tiny LDs in promethin KO cells. (D) Analysis of (C). Bars: mean \pm SEM, $n > 500$ cells/group, 3 experiments. Promethin KO data are pooled from 2 KO pools. Statistics: Mann–Whitney test. (E) Seipin degron cells were delipidated for 3 d, including the last 18 h in the presence of DGAT inhibitors. Cells were treated with IAA as indicated. The inhibitors were washed out, and cells were treated with 200 μ M OA, fixed, stained with anti-promethin antibodies and MDH, and imaged by Airyscan microscopy. Crops of maximum intensity projections of Airyscan z-stacks. Orange arrowheads: LDs with promethin signal; yellow arrowheads: LDs without promethin signal. (F) Analysis of (E). Bars: mean \pm SEM, $n \geq 29$ cells/group, 2 experiments. Statistics: Kruskal–Wallis test followed by Dunn’s test, comparing to no IAA treatment. (G) Immunoblot of seipin levels in seipin degron cells after IAA washout as indicated. Note the recovery of seipin levels upon IAA washout. (H) Analysis of (G). Bars: mean \pm SEM, $n = 3$ biological replicates from 2 experiments. Statistics: 1-way ANOVA followed by Tukey’s post hoc test. (I) Seipin degron cells were delipidated and treated with IAA and OA as indicated. DGAT and SOAT inhibitors were washed out prior to OA addition. Cells were fixed, stained with antibodies, and imaged. Crops from maximum projections of Airyscan z-stacks. Orange arrowheads: seipin foci overlapping with promethin. (J) Analysis of (I). Bars: mean \pm SEM, $n > 60$ cells/group. Data are pooled from 4 experiments, 2 using anti-GFP and 2 using anti-degron tag antibodies for seipin detection. Statistics: Kruskal–Wallis test followed by Dunn’s test. Numerical values for the graphs in (B), (D), (F), (H), and (J) can be found in [S1 Data](#). DGATi, DGAT inhibitor; ER, endoplasmic reticulum; IAA, indole-3-acetic acid; KO, knockout; LD, lipid droplet; MDH, monodansylpentane; mol%, mole percent; OA, oleic acid; SOATi, SOAT inhibitor; TAG, triacylglycerol; WT, wild-type.

<https://doi.org/10.1371/journal.pbio.3000998.g003>

becomes apparent when LDs are induced after a longer (6 h) seipin depletion ([Fig 3C and 3D](#)). Interestingly, we found that loss of promethin sensitized cells to seipin depletion: In promethin KO cells, tiny and supersized LDs appeared when seipin was removed just 30 min prior to LD induction ([Fig 3C and 3D](#)). We also investigated the localization of promethin at nascent LDs under these conditions. In cells containing seipin, virtually all nascent LDs were positive for promethin, and this was also the case if seipin had been depleted for only 30 min prior to LD induction ([Fig 3E and 3F](#)). However, upon longer (6 h) seipin depletion, a large fraction (over 50% on average) of nascent LDs generated did not contain promethin foci ([Fig 3E and 3F](#)).

The above findings are compatible with the idea that the seipin–promethin complex may harbor miniature TAG clusters [44], even in delipidated conditions. Upon seipin removal from promethin-containing cells, these structures may initially be stable and serve as assembly sites for LDs, contributing to the latency in developing the SKO LD phenotype. Upon seipin removal from promethin-deficient cells, these TAG clusters may be destabilized more rapidly, and LD biogenesis proceeds stochastically, with the hallmark of numerous tiny LDs. These data do not rule out other factors, e.g., a more general perturbation of lipid metabolism, that may contribute to the delayed development of the SKO phenotype in the presence of promethin.

TAG facilitates seipin–promethin association

Given that S166D-seipin was dysfunctional in LD biogenesis and failed to colocalize with promethin, we reasoned that the association of TAGs with the seipin oligomer might facilitate seipin–promethin association. However, even prolonged lipid starvation in the presence of neutral lipid synthesizing enzyme inhibitors did not disassemble the promethin–seipin foci ([Fig 3I and 3J](#)). One possibility is that, after initial assembly, promethin–seipin complexes are stable. We therefore investigated the interaction of newly formed seipin oligomers and promethin, taking advantage of seipin degron cells.

Upon IAA washout, seipin levels recovered with an apparent half-time of approximately 16 h, as the cells generated new seipin protein not subjected to degradation ([Fig 3G and 3H](#)). We therefore removed seipin in delipidating conditions (in the presence of neutral lipid synthesizing enzyme inhibitors) and allowed seipin levels to recover for 12 or 24 h ([Fig 3I and 3J](#)). Then, we washed out the inhibitors and pulsed the cells with OA for 10 min to induce TAG synthesis. When seipin foci were synthesized under lipid-poor conditions, a smaller fraction of seipin

overlapped with promethin foci compared to cells where seipin had not been depleted. Remarkably, the 10-min OA pulse increased the fraction of seipin foci overlapping with promethin (Fig 3I and 3J). Similar results were obtained when considering the fraction of promethin overlapping with seipin (S3J and S3K Fig). Together, these data suggest that neutral lipids can facilitate the colocalization of seipin and promethin. We speculate that this may arise from local membrane alterations induced by TAG clustering within the seipin oligomer, providing a favorable environment for promethin association.

Seipin hydrophobic helix provides a seed for TAG nucleation

Our data suggest a model in which seipin attracts TAG from the ER bilayer to its lumen, which then leads to promethin recruitment and, with rising TAG concentration, to LD formation. As our simulations using 2.5 mol% TAG resulted in TAG clustering already in the absence of seipin (Fig 1A), we investigated TAG clustering at a lower concentration (1.25 mol% TAG), comparing systems without seipin, with WT-seipin, and with various seipin mutants. In the absence of seipin, TAG molecules now failed to cluster, whilst WT-seipin facilitated rapid redistribution of TAG to the oligomer lumen (Fig 4A and 4B). Other transmembrane proteins tested did not efficiently catalyze TAG clustering under these conditions (S4 Fig). S166A-seipin facilitated initial TAG clustering, but the process was compromised in the case of S166D- and S165A/S166A-seipin (Fig 4A and 4B). Interestingly, TAG clustering was also achieved by seipin oligomer without its TMDs, suggesting that TMDs are not required for this activity (S4A and S4B Fig). These data suggest that seipin can efficiently concentrate TAG molecules from the surrounding ER bilayer to its lumen, and this is hampered by S166D- or S165A/S166A-seipin.

During LD biogenesis, new TAGs are constantly made via the activity of the ER-resident DGAT enzymes. To mimic this lipogenic condition in simulations, we used the conformation of seipin that hosted a clustered TAG lens in its lumen (30- μ s end point in Fig 1A) as a starting point and replenished the rest of the model ER bilayer with 2.5 mol% TAG. The initially free TAG molecules rapidly started to coalesce with the preexisting TAG cluster, and this was more rapid and efficient in the presence of WT-seipin (Fig 4C and 4D). S166D- and S165A/S166A-seipin failed to catalyze this TAG flux as efficiently as WT-seipin. Interestingly, S166A-seipin was also defective in this (Fig 4D), in line with the observation that S166A was compromised in promoting LD growth (Fig 1E–1H). Together, these data imply that seipin can facilitate TAG flux from nearby ER to a preexisting TAG cluster. Considering the localization of seipin at the ER–LD neck [35], this situation might be reminiscent of an ER-connected nascent LD that grows by additional TAG entering via the seipin disk, as proposed [35,44].

Seipin promotes LD biogenesis at low TAG concentration

The MD simulations suggested that seipin may facilitate nanoscale clustering of TAGs at low TAG concentration. To scrutinize this notion in cells, we treated stringently starved WT and SKO cells with increasing concentrations of OA for short periods of time and analyzed the number of forming LDs. We found that at low OA concentrations, SKO cells formed significantly fewer LDs than WT cells (Fig 4E and 4F). This indicates that seipin is critical to catalyze LD formation at low TAG concentrations.

For comparison, we also performed similar experiments in promethin KO cells. At low OA concentrations, these cells also formed fewer LDs than WT cells (Fig 4E and 4F), but more than SKO cells. Importantly, upon further incubation with high OA concentration, numerous tiny LDs became apparent in SKO cells but not in promethin KO cells (Fig 4E and 4F). Together, these results suggest that while both seipin and promethin are important for LD

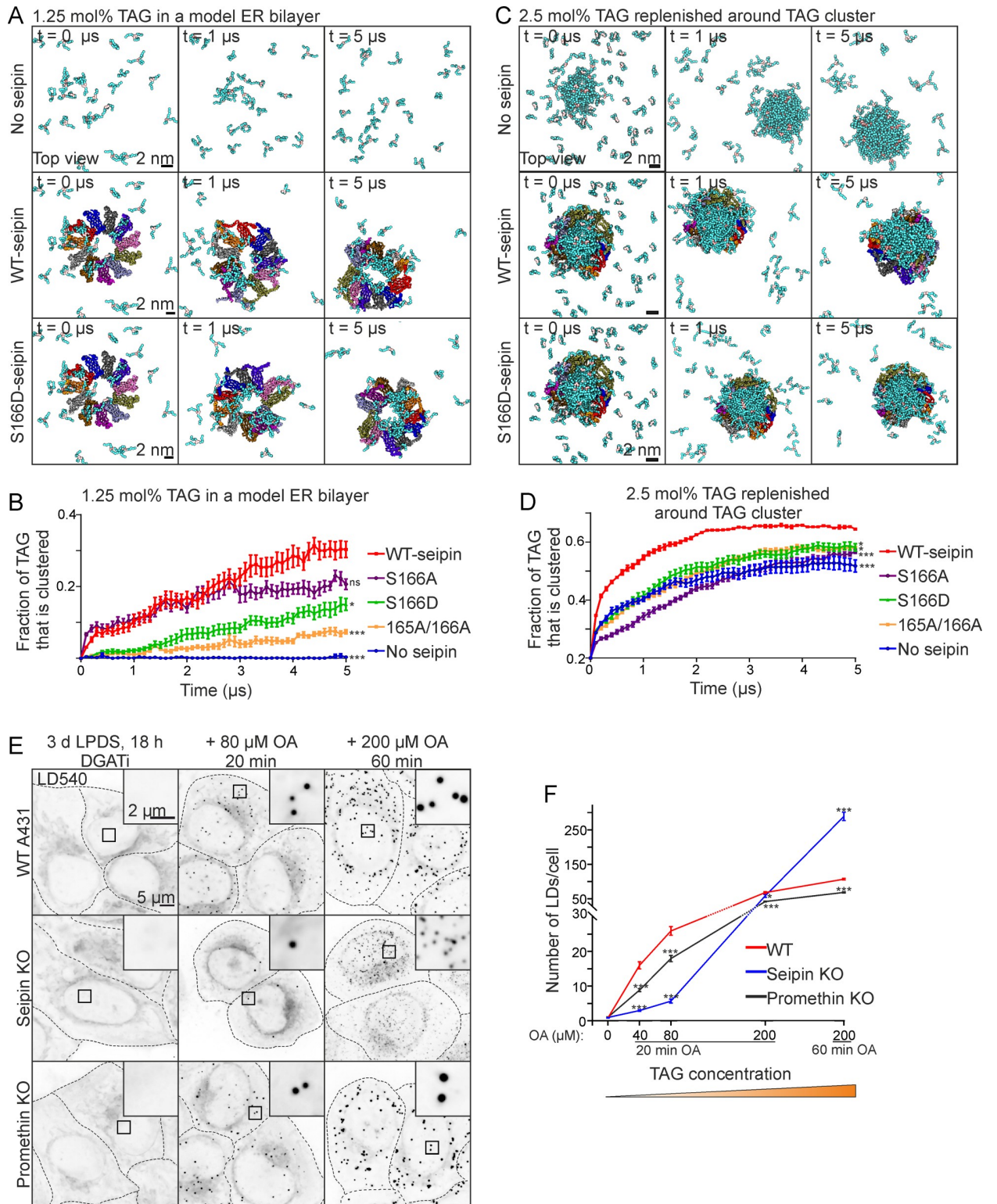


Fig 4. Seipin promotes the nanoscale clustering of TAGs and LD biogenesis at low TAG concentration. (A) Snapshots of coarse-grained simulations with 1.25 mol% TAG in the bilayer. Same color coding as in Fig 1A. (B) Analysis of simulations carried out as in (A). Data points: mean ± SEM, $n = 10$ simulations/system. Statistics are based on the final time points of analysis using Kruskal–Wallis test followed by Dunn’s test, comparing to WT-seipin. (C) Snapshots of coarse-grained simulations with an initial TAG cluster and the rest of the model bilayer replenished with 2.5 mol% TAG (total TAG concentration 4.85 mol%). (D) Analysis of simulations carried out as in (C). Data points: mean ± SEM, $n = 10$

simulations/system. Kruskal–Wallis test followed by Dunn’s test; statistics based on the final time points of analysis, comparing to WT-seipin. (E) Cells were delipidated for 3 d, including 18 h in the presence of DGAT inhibitors. The inhibitors were washed out, and cells were treated with OA as indicated, fixed, stained, and imaged by widefield microscopy. Deconvolved maximum intensity projections of z-stacks. (F) Analysis of (E). Data points: mean \pm SEM, $n > 250$ cells/group, 2 experiments. Statistics: 1-way ANOVA followed by Tukey’s post hoc test, comparison to WT cells. Note that the y-axis is discontinuous. Numerical values for the graphs in (B), (D), and (F) can be found in [S1 Data](#). DGATi, DGAT inhibitor; ER, endoplasmic reticulum; KO, knockout; LD, lipid droplet; LPDS, lipoprotein deficient serum; mol%, mole percent; OA, oleic acid; TAG, triacylglycerol; WT, wild-type.

<https://doi.org/10.1371/journal.pbio.3000998.g004>

formation at low TAG concentration, seipin is required to keep the ER TAG concentration sufficiently low to prevent spontaneous “oiling out” of LDs.

To summarize, our data provide a plausible model of how seipin can attract TAG molecules in the ER. This activity depends on the fidelity of the $\alpha 3$ membrane-anchored helix and a critical S166 therein, with S166 mutations diminishing seipin activity both in silico and in cells. These S166 residues serve as catalysts for concentrating TAGs inside the seipin ring, promoting nanoscale TAG clustering even at minute concentrations. The cylindrical multiunit architecture of seipin is important, providing multiple nucleation sites for TAG clusters. This TAG-attracting propensity of seipin may explain why LDs preferentially form at seipin-defined sites in cells [35,44]. We propose that the TAG-affiliated seipin then recruits promethin, to stabilize the nascent lens through mechanisms yet to be defined. Additional TAGs continuously synthesized in the ER are attracted by seipin and tend to coalesce with the preexisting seipin-trapped TAG nucleus. Such a TAG-harvesting molecular function of seipin likely contributes to its role in preventing ripening and sustaining LD growth [35].

Materials and methods

Materials and reagents

Concentrations in parentheses indicate final concentrations used: rabbit anti-GFP (Abcam, ab290, WB 1:10,000), mouse anti-GFP (Abcam, ab1218, IF 1:250), anti-degron tag (anti-mini-IAA7; Ximbio, 158027, IF 1:500), rabbit anti-TMEM159/promethin (Sigma, HPA063509, IF 1:150, WB 1:500); goat anti-mouse Alexa 488 (Thermo Scientific, A-11001, IF 1:400); goat anti-rabbit Alexa 560 (Thermo Scientific, A11011, IF 1:400); Autodot MDH (Abgent, SM1000a, 0.1 mM); LD540 [49] (synthesized by Princeton BioMolecular Research, 0.1 μ g/ml); DAPI (Sigma, D9542, 10 μ g/ml); SNAP-Cell 647-SiR (New England Biolabs, S9102S, 0.3 μ M); polyethylene glycol (PEG) 1500 (Roche, 50% w/v in 75 mM HEPES); DGAT1 inhibitor (Sigma PZ0207, 5 μ M); DGAT2 inhibitor (Sigma, PZ0233, 5 μ M); SOAT inhibitor (Sigma, S9318, 2 μ g/ml); indole-3-acetic acid (IAA) sodium salt (Santa Cruz Biotechnology, sc-215171, 500 μ M); human fibronectin (Roche Diagnostics, 11051407001); puromycin (Sigma, P8833, 1 μ g/ml); Geneticin (G418, Gibco, 11811–031, 0.6 mg/ml); Zeocin (Thermo Fisher, R25001, 0.2 mg/ml); formaldehyde (Sigma, P-6148, for light microscopy; Electron Microscopy Sciences, EMS-15710, for EM); ECL Clarity (Bio-Rad, 170–5060); ECL Clarity Max substrate (Bio-Rad, 170–5062); saponin (Sigma-Aldrich, S-7900); 12% Mini-PROTEAN TGX Stain-Free gels (Bio-Rad, 161–0185); nitrocellulose membranes (Bio-Rad, 170–4270); Bio-Rad DC protein assay (Bio-Rad, 5000112); 8-well Lab-Tek II #1.5 coverglass slides (Thermo Fisher, 155409); #1.5 polymer μ -slide 8-well and 16-well ibiTreat chambers (Ibidi, 80826 and 81816); HQ SILVER Enhancement Kit (Nanoprobes, 2012); glutaraldehyde (EM-grade, Sigma, G7651); osmium tetroxide (Electron Microscopy Sciences, RT 19130); Epon (TAAB, 812). Other reagents, including cell culture reagents, were from Gibco/Thermo Fisher, Lonza and Sigma, Merck, and Honeywell.

Cell culture

A431 (ATCC CRL-1555) and HEK 293A cells (Invitrogen, R70507) were maintained in Dulbecco's Modified Eagle's Medium (DMEM) containing 10% fetal bovine serum (FBS), penicillin/streptomycin (100 U/ml each), and L-glutamine (2 mM) at 37°C and 5% CO₂.

Plasmids and stable cell lines

A431 SKO cells, generated using CRISPR/Cas9 technology, have been described [34]. The clone used in this study corresponds to S2AB-15 in [34]. End-seipin-GFPx7 cells and end-seipin-SNAPf cells have been described [35]. End-seipin-SNAPf cells stably expressing BFP-KDEL have been described [19]. Seipin degron cells have been described [47]. These cells harbor miniIAA7-GFP at the C-terminus of the endogenous BSCL2/seipin locus and express *AtAFB2*, allowing for efficient depletion of seipin in response to IAA but minimal basal degradation in the absence of IAA.

Promethin KO cells were generated similarly as described [34]. Briefly, WT A431 cells were co-transfected with Cas9 nickase containing the Zeocin selection marker and 2 matching pairs of the sgRNA-expressing plasmids (sgRNA targets: gtttctggccttcaccttgc tgg and ctgtccaagtactgaccac tgg). Twenty-four hours after transfection, cells were placed under Zeocin selection for 48 h. After Zeocin selection, the promethin KO pool was cultured in complete medium in the absence of Zeocin and used for experiments. For promethin KO on top of seipin degron cells, seipin degron cells were treated as described above, but 2 promethin KO pools were made, using the sgRNAs described above (promethin KO-B) as well as another pair of sgRNAs (promethin KO-A; targets: ctggacagccatccgtttc tgg and acccactggagactcataa agg). Both sgRNA pairs were efficient, as assessed by immunoblotting and LD phenotype.

For generating constructs overexpressing seipin with different point mutations, overlapping PCR was used to introduce the point mutations, and to link GFP11x7 tag (from Addgene Plasmid #70224, a gift from Bo Huang [46]) via a flexible linker to the C-terminus of seipin fragments. These fragments were inserted into pmCherry-N1 backbone through Sall and BsrGI restriction sites, resulting in the substitution of the mCherry fragment in the vector. All point mutations were verified by Sanger sequencing. For generating stable SKO cells expressing various seipin point mutants, SKO cells were transfected with pSH-EFIRE5-P-GFP(1–10)optiAAVS1 Safe Harbor integration plasmid (Addgene plasmid #129416 [35]) and pCas9-sgAAVS1-2 (Addgene plasmid #129727 [47]), and a stable pool was selected using puromycin (1 µg/ml puromycin for 6 d, then 5 µg/ml puromycin for 2 d, then cultured further without puromycin). These cells were then transfected with the various point mutant seipin-GFP11X7 constructs, and stable pools were selected using 0.6 mg/ml G418. Cells were FACS-sorted using a BD Influx flow cytometer (BD Biosciences, US) at the HiLIFE Biomedicum Flow Cytometry Unit, University of Helsinki, to enrich cells with GFP fluorescence levels in the range of 0.8- to 2-fold compared to endogenously GFPx7-tagged seipin, using end-seipin-GFPx7 cells [35] as a control. Finally, single clones were isolated using limiting dilution to obtain SKO + WT-seipin-GFPx7, SKO + S166A-seipin-GFPx7, and SKO + S166D-seipin-GFPx7 cells. For transient overexpression (Figs 2E–2H and S2G), seipin tagged with C-terminal EGFP [34] was inserted into pcDNA5/FRT/TO (Thermo Fisher Scientific) through HindIII/NotI sites. The S166D point mutation was introduced by overlap PCR.

Transfection, lipid and IAA treatments, SNAP-labeling, and cell fusion

Transfection of plasmids was carried out using Lipofectamine LTX with PLUS Reagent or XtremeGENE HP DNA according to manufacturer's instructions. Cells were delipidated by culturing in serum-free medium supplemented with 5% LPDS for indicated times. Where

indicated, for more stringent delipidation, cells were additionally incubated with DGAT1, DGAT2, and SOAT inhibitors. “DGAT inhibitors” indicates both DGAT1 and DGAT2 inhibitors. These inhibitors were washed out by 4 washes with PBS. For LD induction, cells were supplemented with the indicated concentration of OA (OA in complex with BSA in 8:1 molar ratio prepared in serum-free DMEM as described in [50]). For seipin depletion, IAA was added to the medium. For IAA washout, cells were washed with PBS 4 times and cultured in a medium without IAA. SNAP-labeling was done for 5 min at +37°C, the label SNAP-Cell 647-SiR was applied in 5% LPDS containing medium followed by 3 washes with PBS. SNAP-labeling was performed 4 h prior to imaging experiments. Cells were fused with PEG 1500 for 1 min, followed by 4 washes with PBS and further incubation in complete medium with OA.

Immunofluorescence staining

Immunofluorescence was performed as described [35], using 0.1% saponin for permeabilization and 10% FBS for blocking and antibody dilutions.

Immunoblotting

Cells were lysed into RIPA buffer (1% IGEPAL CA-630, 0.1% SDS in TBS) containing protease inhibitors. After lysis, lysate was cleared by centrifugation at 16,000g for 10 min at +4°C, and the supernatant was collected. Protein concentrations were measured using DC protein assay. For anti-promethin immunoblotting, samples in 1× Laemmli buffer were incubated at room temperature (RT) for 15 min, heated at +70°C for 5 min, and cooled down at RT for 30 min prior to loading onto gels. For anti-GFP immunoblotting, samples in 1× Laemmli buffer were kept on ice prior to loading onto gels without heating. Equal amounts of protein were loaded onto 12% Mini-PROTEAN TGX Stain-Free gels and transferred onto PVDF membrane. Membranes were blocked with 5% milk in TBS containing 0.1% Tween-20 for 1 h at RT, and probed with primary antibodies at +4°C overnight. After washing with TBS containing 0.1% Tween-20, membranes were incubated with secondary antibodies for 1–2 h at RT. Membranes were washed, incubated with ECL or ECL Clarity Max substrate, and imaged with a ChemiDoc Imaging System (Bio-Rad). Band intensities were quantified in ImageJ FIJI and normalized to total protein content quantified with the Stain-Free technology (Bio-Rad). Stain-Free total protein signals are shown as loading controls in the figures. Uncropped immunoblots are found in [S1 Raw Images](#).

Light microscopy and image analysis

Live and fixed cell imaging. Cells were seeded onto Ibidi μ -slide 8- or 18-well ibiTreat chambers or #1.5 coverglasses for widefield microscopy, or 8-well Lab-Tek II #1.5 coverglass slides for Airyscan microscopy, the latter coated with 10 mg/ml fibronectin. All live cell imaging experiments were performed at +37°C, 5% CO₂ in FluoroBrite DMEM supplemented with 10% FBS, penicillin/streptomycin (100 U/ml each), and L-glutamine (2 mM). For light microscopy of fixed cells, cells were washed with PBS and fixed with 4% PFA in 250 mM HEPES (pH 7.4), 100 mM CaCl₂, and 100 mM MgCl₂ for 20 min, followed by quenching in 50 mM NH₄Cl for 10 min and 3 washes with PBS. For the data in [Figs 1E, 1F, 3E, 3F and S1B](#), LDs were stained with MDH at RT for 10 min, followed by 3 washes with PBS. For the data in [Figs 3C, 3D, 4E and 4F](#), nuclei were stained with DAPI for 10 min at RT, and, after 3 washes with PBS, LDs were stained with LD540 for 20 min at RT. LD dyes and DAPI were diluted in PBS. For the data in [S3B–S3D Fig](#), samples were mounted with Mowiol-DABCO.

Fixed and live cell Airyscan imaging. Cells were imaged with a Zeiss LSM 880 confocal microscope equipped with Airyscan (Fast) detector using a 63× Plan-Apochromat oil

objective, NA 1.4. After fixing, cells were kept in PBS until imaging and stained for LDs immediately prior to imaging. Imaging was done in Airyscan super resolution mode. The Airyscan detector was adjusted regularly between acquisitions. For the data in Figs 1E–1H, 3A, 3B, 3E, 3F, 3I, 3J and S1B–S1D, z-stacks of cells were imaged using Airyscan microscopy. For the data in Fig 2E, single z-planes were captured in live cells. For the data in Fig 1H, fused cells containing both seipin-GFPx7 and seipin-SNAPf signal were imaged.

Fixed and live cell widefield imaging. Cells were imaged with a Nikon Eclipse Ti-E microscope equipped with a 60× Plan-Apochromat λ oil objective, NA 1.4, and a 1.5 zoom lens, Nikon Perfect Focus System 3, Hamamatsu Flash 4.0 V2 scientific CMOS camera, and Okolab stage top incubator system. For the data in S2G Fig, a single z-plane was imaged every 30 min for 10 h. For the data in Figs 3C, 3D, 4E, 4F and S3I, z-stacks spanning the whole cell (step size 0.3 μ m) were acquired.

Image processing. Airyscan images and videos were Airyscan-processed using the Zeiss Zen software package with identical (default) settings for all acquisitions. Deconvolution of widefield images was performed with Huygens software (Scientific Volume Imaging) using iterative classic maximum likelihood estimation. For downstream image analysis, z-stacks were maximum intensity projected using ImageJ FIJI or Matlab. Brightness, contrast, and scale bars were adjusted in ImageJ FIJI and Corel Draw 2017 (64 bit).

Image analysis. For all LD analyses, except Fig 3C and 3D, LDs were segmented with Ilastik [51,52] using pixel and object classification mode, and final binary images were used for analysis. Subsequent cell segmentation was performed with CellProfiler [53], in a hierarchical manner, as previously reported [54]. For the data in Figs 3C, 3D, 4E, 4F and S3I, cell nuclei were detected using the DAPI images with the Otsu adaptive thresholding method. Touching nuclei were separated by built-in intensity methods. The cytoplasm was detected by utilizing the faint cellular background of the DAPI channel, using intensity propagation based on the Otsu adaptive thresholding method and the identified nuclei from the first step as a seed point. Finally, LDs were detected using static Otsu thresholding of the binary LD images generated in Ilastik or directly in CellProfiler (for the data in Figs 3C, 3D and S3I), using the CellProfiler module DetectAllDroplets [35]. Subsequent feature analysis, including analysis of LD size distributions and total LD numbers/cell, was done with CellProfiler and custom Matlab software generated for post-processing reported in [35]. For the data in Fig 1E and 1F, images were manually cropped so that each image was from 1 cell and separate cell segmentation was not necessary, and LD analysis was performed as described above. For the data in Figs 3A, 3B, 3E, 3F, 3I, 3J, S3F, S3J and S3K, each image was of a peripheral section of a single cell, and cell boundary segmentation was performed in CellProfiler using the faint background of antibody or LD staining. For the data in Figs 3A, 3B, 3I, 3J, S3J and S3K, seipin and promethin foci were segmented with Ilastik using pixel and object classification mode, and their overlap was analyzed using CellProfiler and custom Matlab software as described above. Fig 3E and 3F was analyzed similarly, except that promethin and LD overlap was analyzed. In all cases, structures were considered overlapping if they overlapped by at least 1 pixel. For the data in S3D Fig, cells were manually outlined, and the mean intensity of promethin staining per cell (after background subtraction) was analyzed in ImageJ FIJI. For the data in Fig 1H, LDs were first segmented using Ilastik. Then, a static threshold was applied to the end-seipin-SNAPf channel, and the sizes of thresholded LDs overlapping or not with seipin-SNAPf foci were analyzed in ImageJ FIJI [55].

Electron microscopy

Cells grown on fibronectin-coated coverslips were fixed with 2.5% glutaraldehyde in sodium cacodylate buffer (pH 7.4) supplemented with 2 mM CaCl₂ for 25 min at RT. After washing,

the cells were post-fixed with (non-reduced) 1% osmium tetroxide in 0.1 M sodium cacodylate buffer (pH 7.4) for 1 h at RT, dehydrated in an ethanol series, and flat embedded as described previously [56]. Ultrathin sections were post-stained with uranyl acetate and lead citrate, and imaged using a Jeol JEM-1400 microscope equipped with Orius SC 1000B camera (Gatan).

Electron tomography. For immunoelectron tomography (Fig 2H), the specimens were prepared as described in [34]. Briefly, after PLP fixation [57] and permeabilization with 0.01% saponin, the cells were labeled with anti-GFP antibody for 1 h and nano-gold-conjugated anti-rabbit FAB fragments for 1 h, post-fixed with 1% glutaraldehyde, and quenched with 50 mM glycine. Nano-gold particles were then intensified for 2 min using the HQ SILVER Enhancement Kit followed by gold toning in subsequent incubations in 2% sodium acetate, 0.05% HAuCl₄, and 0.3% sodium thiosulfate prior to osmication, dehydration, and flat embedding as described in [56]. A 230-nm-thick section cut parallel to the cover slip was subjected to electron tomography at a nominal magnification of 19,000 \times , providing a 2 \times binned pixel size of 1.2 nm, using a Tecnai FEG 20 microscope (Thermo Fisher Scientific, formerly FEI) operated at 200 kV. The alignment of the tilt series as well as reconstruction (SIRT technique using 14 iterations) were done with the IMOD software package [58] (version 4.10.32). Segmentation and visualization were done using MIB [59] (version 2.601) and Amira (VSG, FEI) (version 5.3.2), respectively. The immunolabeling is not shown, as the labeling was clearly denser at the outskirts and edges of the S166D-induced ER sacs, suggesting that steric hindrance may prevent diffusion of the antibodies to these structures.

Computational methods

Protein modeling. Seipin oligomer was modeled as an all-atom description using the cryo-EM structure of human seipin (PDB ID: 6DS5 [31]). The structure of an individual seipin monomer comprised of amino acids (aa.) 25–263 corresponds to the N-terminal transmembrane helix (aa. 27–47), topological domain (aa. 48–242), and C-terminal transmembrane helix (aa. 243–263). The terminal topological domains (aa. 1–24 and 264–398) were not modeled into the seipin structure. The TMDs of the protein (corresponding to aa. 25–47 and 243–263) and the missing segments of the luminal domain (corresponding to aa. 48–59 and 220–242) were built into the cryo-EM structure using the PyMol software. The transmembrane region of the protein was modeled as a regular right-handed alpha-helix. Residue N88 was N-glycosylated (Man α 1-6(Man α 1-3)Man β 1-4GlcNAc β 1-4GlcNAc β 1-Asn).

Building the simulation system. Continuing at atomic resolution, a multi-component lipid bilayer (S1 Table) mimicking the lipid profile found in the ER [60] was constructed around the seipin oligomer. All lipids were randomly distributed in the membrane plane. The transmembrane distribution of TAGs was symmetric. For other lipids, the transmembrane lipid distribution in the ER is not well known. Some studies have reported that it is asymmetric [61,62], while there are also views in favor of a symmetric distribution [63]. In the present work, for the sake of completeness, we considered both options: an asymmetric transmembrane lipid distribution that was tuned from previous simulation studies [64] and a symmetric distribution. The results presented in this article are based on the asymmetric distribution, unless otherwise noted, but the results based on a symmetric distribution are consistent with those based on the asymmetric distribution. Lateral pressure was applied to ensure proper packing of the lipids around the oligomer structure. The TMDs and the α 2– α 3 helical segment (aa. 154–170) of the protein were embedded within the bilayer. The system was solvated (full hydration) and counter ions were added to neutralize the system. Additionally, 0.15 M KCL was used to mimic the physiological salt concentration in the cytosol.

For TAGs, the objective was to track non-equilibrium diffusion and clustering processes where initially random distributions of TAGs self-assemble spontaneously to form TAG-rich clusters. Given this, the simulation systems equilibrated during the clustering processes.

Simulation parameters. Simulations of both all-atom and coarse-grained model systems (S2 Table) were carried out using the GROMACS simulation package, version 2016.4 [65]. In all-atom simulations, we used the CHARMM36 force field [66–69] for the proteins, lipids, ions, and TAGs. For water, the force field used was CHARMM TIP3P. The simulation systems were first energy minimized and pre-equilibrated under constant temperature and pressure for 1 ns. Temperature was maintained at 310 K using the Nose–Hoover thermostat [70] with a coupling constant of 0.5 ps. Pressure was maintained semi-isotropically at 1 atm using the Parrinello–Rahman barostat [71] with a coupling constant of 2 ps. The time step used for integrating the equations of motion was 2 fs. The neighbor list was updated every 10 steps using the Verlet cutoff scheme. The LINCS algorithm [72] was used to constrain the motion of covalently bonded hydrogen bonds. Short-range interactions (electrostatic and van der Waals) were cut off at 1.0 nm. The long-range component of electrostatic interactions was calculated using the particle mesh Ewald (PME) method [73]. For every system, production simulations of 1- μ s length were performed in 2 replicates.

In coarse-grained simulations, a model consistent with the MARTINI framework (version 2.2) [72,74,75] was first generated from the atomistic protein model using the martinize.py script (<http://cgmartini.nl/index.php/tools2/proteins-and-bilayers>). The residue N88 was not glycosylated in the coarse-grained model of seipin. The systems were again first energy minimized and pre-equilibrated under constant temperature and pressure for 10 ns. Temperature was maintained at 310 K by the V-rescale thermostat [76], and pressure was maintained semi-isotropically at 1 atm using the Parrinello–Rahman barostat. The standard MARTINI water model was used with a relative dielectric constant of 15. A cutoff of 1.1 nm was used for Coulomb and van der Waals interactions. The integration time step was chosen as 20 fs. Production simulations of 5 μ s each were carried out in 10 replicates starting from different initial conditions. Further, to foster the sampling of clustering of TAGs at longer time scales, 3 sets from each of the coarse-grained systems with a TAG concentration of 2.5 mol% were randomly chosen and extended to 30 μ s.

The simulations of seipin were complemented by coarse-grained simulations of other membrane proteins that do not play a known role in LD biogenesis: β 2-adrenergic receptor (B2AR) (PDB ID: 3D4S [77]) and sigma-1 receptor (S1R) (PDB ID: 5HK1 [78]). The simulation protocol was the same as that used for seipin.

Analysis of simulation data. All analysis was carried out using standard GROMACS tools. The mean curvature of the leaflets was calculated using *g_lomepro* [79]. VMD [80] was used for visualizing the simulations and rendering images.

Average TAG occupancies were calculated for each amino acid residue in the seipin oligomer (Fig 1C) as follows: For each nanosecond, the smallest distance between the selected amino acid residue and all TAG molecules in the membrane was computed. The residue was considered to interact with TAG if the smallest distance was 0.5 nm or less. This analysis was carried out separately for 0–1 and 4–5 μ s of simulation time, over all simulation repeats of the same system, and separately for every residue of seipin, thus giving an average occupancy number for each residue. An occupancy value of 1 indicates that the selected amino acid residue always interacted with TAG, while a value of 0 indicates that the amino acid residue never experienced interactions with TAG.

To calculate the fraction of TAGs clustered in a bilayer (Fig 4B and 4D), we calculated the smallest distance between a chosen TAG and the rest of the TAG molecules. The chosen TAG molecule was considered to interact with other TAGs if the smallest distance was 0.5 nm or

less, and was considered to be part of a cluster if it interacted with at least 2 other TAG molecules. Therefore, the fraction of TAGs clustered in a bilayer excludes monomeric and dimeric TAGs.

Short-time diffusion coefficient D for TAGs inside the seipin complex (Fig 2A) was calculated using a technique discussed by Vuorela et al. [81]. For a given molecule, one records the 2D (in the plane of the membrane) displacement (Δr) during a time interval Δt . When the molecule diffuses over a long period of time, one finds the distribution of these displacements, $P(\Delta r)$, which can be fitted to the theoretical distribution [81]. The fitting yields a value for the short-time diffusion coefficient D . Since the analysis was made over a period of $\Delta t = 1$ ns, this analysis yields a diffusion coefficient that characterizes diffusive behavior in the nanometer-scale, and is thus able to document TAG binding for S166 and its mutants.

Statistics

Statistical analysis was performed with Graphpad Prism (Graphpad Software), using statistical tests as indicated in the figure legends. p -Values < 0.05 were considered significant. Throughout the figure legends: * $p < 0.05$, ** $p < 0.005$, *** $p < 0.0005$.

Supporting information

S1 Data. Numerical data for graphs in figures. Each spreadsheet contains the numerical raw data of 1 figure panel as indicated.
(XLSX)

S1 Fig. Supporting information for Fig 1. (A) Side view of the seipin oligomer in the model ER bilayer. The model was based on the cryo-EM structure of human seipin, and the TMDs were modeled. The lipid composition was modeled to match that reported for the ER. (B) A431 SKO cells stably expressing the indicated plasmids were delipidated for 3 d and treated with 200 μM OA for 1 h. Cells were fixed, LDs stained, and cells imaged by Airyscan microscopy. Orange arrowheads: tiny LDs; yellow arrowheads: supersized LDs. (C) Related to Fig 1E and 1F. Indicated cell lines were delipidated for 3 d and treated with OA for 1 h. Cells were fixed, LDs stained, and cells imaged by Airyscan microscopy. The number of seipin foci per cell area was analyzed and plotted. $n = 35$ cells for end-seipin-GFPx7, >60 cells/group for the others, 3–4 experiments. (D) Exemplary crops of nearby LDs from cells treated as indicated. Green arrowheads: WT-, S166A-, or S166D-seipin-GFPx7-associated LDs; magenta arrowheads: end-seipin-SNAPf-associated LDs. See Fig 1H for analysis of the data. Numerical values for the graph in (C) can be found in S1 Data.
(TIF)

S2 Fig. Supporting information for Fig 2. (A) Snapshots of atomistic simulations showing the relative position of $\alpha 2$ – $\alpha 3$ helices (pink) with respect to the head group region of the PLs in the bilayer (represented by phosphate atoms shown as yellow spheres) at the beginning (0 μs) and end (1 μs) of simulation. The system consists of 2.5 mol% TAG randomly distributed in the bilayer around the seipin oligomer. The transmembrane helices and luminal domain are shown in white (transparent). The TAGs are shown in cyan (transparent). (B) Center of mass distance between the residue 166 (all) and the phosphate atom of PLs in the luminal leaflet of the bilayer over the simulation period for the systems shown in (A). (C) Snapshots of atomistic simulations showing the relative position of $\alpha 2$ – $\alpha 3$ helix with respect to the head group region of the PLs in the bilayer at the beginning (0 μs) and end (1 μs) of simulation. The system consists of 2.5 mol% TAG clustered within the lumen of the seipin oligomer. Coloring as in (A). (D) Center of mass distance between residue 166 (all) and the phosphate

atom of PLs in the luminal leaflet of the bilayer over the simulation period for the systems shown in (C). (E) Snapshots of atomistic simulations. Left snapshot shows the membrane deformation (depicted by the invagination of phosphate atoms from the cytosolic leaflet into the bilayer) in the S166D-seipin system. All S166D residues were then protonated (0 μ s) and simulated. Right snapshot at the end of the 200-ns simulation shows that the deformation has relaxed. Coloring as in (A). (F) Minimum distance between the protonated S166D residue 166 (all) and phosphate atoms of the PLs in the cytosolic leaflet of the bilayer over a simulation period of 200 ns. Similar data for wild-type S166 residue is shown for reference. (G) HEK 293A cells were transfected with S166D-seipin-GFP and imaged live by widefield microscopy. A single cell is shown over time; orange arrowheads indicate smaller GFP foci, which upon rising fluorescence levels coalesce to a larger membranous aggregate (green arrowheads).

Numerical values for the graphs in (B), (D), and (F) can be found in [S1 Data](#).

(TIF)

S3 Fig. Supporting information for Fig 3. (A) Representative immunoblot of WT A431 cells and promethin KO cell pool using anti-promethin antibody. Asterisk indicates unspecific band. Note both monomer-sized (17 kDa) and larger (>250 kDa) specific bands. (B) End-seipin-GFPx7 cells and promethin KO cells were co-plated, fixed, and stained with anti-promethin antibodies. Asterisks indicate promethin KO cells that have not been engineered to harbor seipin-GFPx7. Note bright promethin staining in the end-seipin-GFPx7 cells. Maximum projections of widefield *z*-stacks. (C) Cells were cultured in complete medium or additionally treated with 200 μ M OA for 18 h, fixed, and stained with anti-promethin antibodies. (D) Analysis of (C). Bars: mean \pm SEM, $n = 71$ –180 cells/group, representative experiment repeated once with similar results. Statistics: Mann–Whitney test. (E) End-seipin-GFPx7 cells were treated with 200 μ M OA for 18 h, fixed, and stained with anti-promethin antibodies and MDH. Maximum projection of 2 Airyscan *z*-slices 210 nm apart. (F) In relation to [Fig 3B](#), the fraction of seipin foci overlapping with promethin foci is plotted relative to the number of seipin foci per cell area. A value of 1 in number of seipin foci per cell area corresponds to the mean number of seipin foci per cell area detected in end-seipin-GFPx7 cells in [S1C Fig](#). (G) Immunoblots of seipin degran cells with or without promethin KO treated with IAA. (H) Analysis of (F). Bars: mean \pm SEM, $n = 3$ –6 replicates/group, 2 experiments. Promethin KO data are pooled from KO-A and KO-B pools. Statistics: Mann–Whitney test. (I) In relation to [Fig 3C and 3D](#), an additional representation of the “No IAA” data of that panel. Seipin degran cells \pm promethin KO were delipidated for 3 d and treated with OA for 1 h as in [Fig 3C](#), and LDs were analyzed. Bars: mean \pm SEM, $n > 500$ cells/group, 3 experiments. Promethin KO data are pooled from KO-A and KO-B pools. Statistics: Mann–Whitney test. (J) Additional analysis of the data in [Fig 3I and 3J](#). Cells were treated as in [Fig 3I](#), and the fraction of promethin foci overlapping with seipin foci was analyzed. Bars: mean \pm SEM, $n > 60$ cells/group, 4 experiments. Statistics: Kruskal–Wallis test followed by Dunn’s test. (K) Additional analysis of the data in [Fig 3I and 3J](#). The number of seipin or promethin foci per cell area is plotted, normalized to the number of seipins or promethins per cell area in the “No IAA” sample. Bars: mean \pm SEM, $n > 60$ cells/group, 4 experiments. Numerical values for the graphs in (D), (F), (H), (I), (J), and (K) can be found in [S1 Data](#).

(TIF)

S4 Fig. Supporting information for Fig 4. (A) In relation to [Fig 4A](#). Snapshots of coarse-grained simulations with 1.25 mol% TAG in the bilayer. Results are shown for 2 additional integral membrane proteins to demonstrate their TAG affinities. The color coding is as in [Fig 1A](#). Snapshots of “No seipin” and “WT seipin” are the same as in [Fig 4A](#). (B) Analysis of (A). Data points: mean \pm SEM, $n = 10$ simulations/system. Data for “No seipin” and “WT seipin”

are same as in Fig 4B. Statistics are based on the final time points of analysis using Kruskal–Wallis test followed by Dunn’s test, comparing against no seipin. (C) Additional analysis of the data in Fig 4B and (B). Total surface area of protein exposed to membrane lipids was calculated using GROMACS tool sasa. Data points: mean \pm SEM; data is from 10 simulations/system. Whilst membrane proteins are expected to reduce the mobility of nearby lipids relative to the membrane exposed protein surface area (the so called blocking effect), this does not explain the TAG-clustering effect of WT seipin. Numerical values for the graphs in (A), (B), and (C) can be found in S1 Data.

(TIF)

S1 Raw Images. The file contains original uncropped immunoblots.

(PDF)

S1 Table. Lipid composition of the membrane used in seipin oligomer simulations. The membrane was comprised of 13 different lipid species with molar concentrations identified in the table.

(DOCX)

S2 Table. Systems explored through atomistic and coarse-grained simulation models.

(DOCX)

Acknowledgments

We thank Anna Uro and Suvi Saarnio for excellent technical assistance, and Fabio Lolicato for providing the all-atom force field for TAG. We thank the Helsinki Institute of Life Science (HiLIFE) Light Microscopy Unit, HiLIFE Electron Microscopy Unit, HiLIFE Flow Cytometry Unit, and Biocenter Finland for infrastructure support. We thank CSC–IT Center for Science (Espoo, Finland) and the Finnish Grid and Cloud Infrastructure (FGCI) for computing resources.

Author Contributions

Conceptualization: Xavier Prasanna, Veijo T. Salo, Ilpo Vattulainen, Elina Ikonen.

Formal analysis: Xavier Prasanna, Veijo T. Salo, Helena Vihinen.

Funding acquisition: Eija Jokitalo, Ilpo Vattulainen, Elina Ikonen.

Investigation: Xavier Prasanna, Veijo T. Salo, Shiqian Li, Katharina Ven, Helena Vihinen, Ilpo Vattulainen.

Methodology: Xavier Prasanna, Veijo T. Salo, Shiqian Li, Katharina Ven, Helena Vihinen, Eija Jokitalo, Ilpo Vattulainen, Elina Ikonen.

Project administration: Eija Jokitalo, Ilpo Vattulainen, Elina Ikonen.

Resources: Eija Jokitalo, Ilpo Vattulainen, Elina Ikonen.

Supervision: Eija Jokitalo, Ilpo Vattulainen, Elina Ikonen.

Visualization: Xavier Prasanna, Veijo T. Salo, Helena Vihinen, Ilpo Vattulainen, Elina Ikonen.

Writing – original draft: Veijo T. Salo, Elina Ikonen.

Writing – review & editing: Xavier Prasanna, Veijo T. Salo, Shiqian Li, Katharina Ven, Helena Vihinen, Eija Jokitalo, Ilpo Vattulainen, Elina Ikonen.

References

1. Olzmann JA, Carvalho P (2019) Dynamics and functions of lipid droplets. *Nat Rev Mol Cell Biol.* 20:137–55. <https://doi.org/10.1038/s41580-018-0085-z> PMID: 30523332
2. Henne WM, Reese ML, Goodman JM (2018) The assembly of lipid droplets and their roles in challenged cells. *EMBO J.* 37:e98947. <https://doi.org/10.15252/emboj.201898947> PMID: 29789390
3. Jackson CL (2019) Lipid droplet biogenesis. *Curr Opin Cell Biol.* 59:88–96. <https://doi.org/10.1016/j.ceb.2019.03.018> PMID: 31075519
4. Henne M, Goodman JM, Hariri H (2020) Spatial compartmentalization of lipid droplet biogenesis. *Biochim Biophys Acta Mol Cell Biol Lipids.* 1865:158499. <https://doi.org/10.1016/j.bbalip.2019.07.008> PMID: 31352131
5. Walther T, Chung J, Farese RV Jr (2017) Lipid droplet biogenesis. *Annu Rev Cell Dev Biol.* 33:491–510. <https://doi.org/10.1146/annurev-cellbio-100616-060608> PMID: 28793795
6. Choudhary V, Ojha N, Golden A, Prinz WA (2015) A conserved family of proteins facilitates nascent lipid droplet budding from the ER. *J Cell Biol.* 211:261–71. <https://doi.org/10.1083/jcb.201505067> PMID: 26504167
7. Kassar A, Herms A, Fernández-Vidal A, Bosch M, Schieber NL, Reddy BJN, et al. (2013) Acyl-CoA synthetase 3 promotes lipid droplet biogenesis in ER microdomains. *J Cell Biol.* 203:985–1001. <https://doi.org/10.1083/jcb.201305142> PMID: 24368806
8. Ohsaki Y, Cheng J, Suzuki M, Fujita A, Fujimoto T (2008) Lipid droplets are arrested in the ER membrane by tight binding of lipidated apolipoprotein B-100. *J Cell Sci.* 121:2415–22. <https://doi.org/10.1242/jcs.025452> PMID: 18577578
9. Salo VT, Ikonen E (2019) Moving out but keeping in touch: contacts between endoplasmic reticulum and lipid droplets. *Curr Opin Cell Biol.* 57:64–70. <https://doi.org/10.1016/j.ceb.2018.11.002> PMID: 30476754
10. Schuldiner M, Bohnert M (2017) A different kind of love—lipid droplet contact sites. *Biochim Biophys Acta Mol Cell Biol Lipids.* 1862:1188–96. <https://doi.org/10.1016/j.bbalip.2017.06.005> PMID: 28627434
11. Enkavi G, Javanainen M, Kulig W, Róg T, Vattulainen I (2019) Multiscale simulations of biological membranes: the challenge to understand biological phenomena in a living substance. *Chem Rev.* 119:5607–774. <https://doi.org/10.1021/acs.chemrev.8b00538> PMID: 30859819
12. Hollingsworth SA, Dror RO (2018) Molecular dynamics simulation for all. *Neuron.* 99:1129–43. <https://doi.org/10.1016/j.neuron.2018.08.011> PMID: 30236283
13. Khandelia H, Duelund L, Pakkanen KI, Ipsen JH (2010) Triglyceride blisters in lipid bilayers: implications for lipid droplet biogenesis and the mobile lipid signal in cancer cell membranes. *PLoS ONE.* 5:e12811. <https://doi.org/10.1371/journal.pone.0012811> PMID: 20877640
14. Chorlay A, Monticelli L, Verissimo Ferreira J, Ben M'barek K, Ajjaji D, Wang S, et al. (2019) Membrane asymmetry imposes directionality on lipid droplet emergence from the ER. *Dev Cell.* 50:25–42.e7. <https://doi.org/10.1016/j.devcel.2019.05.003> PMID: 31155466
15. Ben M'barek K, Ajjaji D, Chorlay A, Vanni S, Forêt L, Thiam AR (2017) ER membrane phospholipids and surface tension control cellular lipid droplet formation. *Dev Cell.* 41:591–604.e7. <https://doi.org/10.1016/j.devcel.2017.05.012> PMID: 28579322
16. Choudhary V, Golani G, Joshi AS, Cottier S, Schneiter R, Prinz WA, et al. (2018) Architecture of lipid droplets in endoplasmic reticulum is determined by phospholipid intrinsic curvature. *Curr Biol.* 28:915–26.e9. <https://doi.org/10.1016/j.cub.2018.02.020> PMID: 29526591
17. Thiam AR, Forêt L (2016) The physics of lipid droplet nucleation, growth and budding. *Biochim Biophys Acta Mol Cell Biol Lipids.* 1861:715–22. <https://doi.org/10.1016/j.bbalip.2016.04.018> PMID: 27131867
18. Zoni V, Nieto V, Endter LJ, Risselada HJ, Monticelli L, Vanni S (2019) To bud or not to bud: a perspective on molecular simulations of lipid droplet budding. *Front Mol Biosci.* 6:2017–20. <https://doi.org/10.3389/fmolb.2019.00124> PMID: 31799255
19. Santinho A, Salo VT, Chorlay A (2020) Membrane curvature catalyzes lipid droplet assembly. *Curr Biol.* 30:2481–94.e6. <https://doi.org/10.1016/j.cub.2020.04.066> PMID: 32442467
20. Prévost C, Sharp ME, Kory N, Lin Q, Voth GA, Farese RV, et al. (2018) Mechanism and determinants of amphipathic helix-containing protein targeting to lipid droplets. *Dev Cell.* 44:73–86.e4. <https://doi.org/10.1016/j.devcel.2017.12.011> PMID: 29316443
21. Bacle A, Gautier R, Jackson CL, Fuchs PFJ, Vanni S (2017) Interdigitation between triglycerides and lipids modulates surface properties of lipid droplets. *Biophys J.* 112:1417–30. <https://doi.org/10.1016/j.bpj.2017.02.032> PMID: 28402884

22. Čopič A, Antoine-Bally S, Giménez-Andrés M, La Torre Garay C, Antonny B, Manni MM, et al. (2018) A giant amphipathic helix from a perilipin that is adapted for coating lipid droplets. *Nat Commun.* 9:1332. <https://doi.org/10.1038/s41467-018-03717-8> PMID: 29626194
23. Fei W, Shui G, Gaeta B, Du X, Kuerschner L, Li P, et al. (2008) Fld1p, a functional homologue of human seipin, regulates the size of lipid droplets in yeast. *J Cell Biol.* 180:473–82. <https://doi.org/10.1083/jcb.200711136> PMID: 18250201
24. Szymanski KM, Binns D, Bartz R, Grishin NV, Li W, Agarwal AK, et al. (2007) The lipodystrophy protein seipin is found at endoplasmic reticulum lipid droplet junctions and is important for droplet morphology. *Proc Natl Acad Sci U S A.* 104:20890–5. <https://doi.org/10.1073/pnas.0704154104> PMID: 18093937
25. Chen W, Yechoor VK, Chang BH-J, Li MV, March KL, Chan L (2009) The human lipodystrophy gene product Berardinelli-Seip congenital lipodystrophy 2/seipin plays a key role in adipocyte differentiation. *Endocrinology.* 150:4552–61. <https://doi.org/10.1210/en.2009-0236> PMID: 19574402
26. Payne VA, Grimsey N, Tuthill A, Virtue S, Gray SL, Nora ED, et al. (2008) The human lipodystrophy gene BSCL2/seipin may be essential for normal adipocyte differentiation. *Diabetes.* 57:2055–60. <https://doi.org/10.2337/db08-0184> PMID: 18458148
27. Magré J, Delépine M, Khallouf E, Gedde-Dahl T, Van Maldergem L, Sobel E, et al. (2001) Identification of the gene altered in Berardinelli-Seip congenital lipodystrophy on chromosome 11q13. *Nat Genet.* 28:365–70. <https://doi.org/10.1038/ng585> PMID: 11479539
28. Windpassinger C, Auer-Grumbach M, Irobi J, Patel H, Petek E, Hörl G, et al. (2004) Heterozygous missense mutations in BSCL2 are associated with distal hereditary motor neuropathy and Silver syndrome. *Nat Genet.* 36:271–6. <https://doi.org/10.1038/ng1313> PMID: 14981520
29. Ito D, Suzuki N (2009) Seipinopathy: a novel endoplasmic reticulum stress-associated disease. *Brain.* 132:8–15. <https://doi.org/10.1093/brain/awn216> PMID: 18790819
30. Guillén-Navarro E, Sánchez-Iglesias S, Domingo-Jiménez R, Victoria B, Ruiz-Riquelme A, Rábano A, et al. (2013) A new seipin-associated neurodegenerative syndrome. *J Med Genet.* 50(6):401–9. <https://doi.org/10.1136/jmedgenet-2013-101525> PMID: 23564749
31. Yan R, Qian H, Lukmantara I, Gao M, Du X, Yan N, et al. (2018) Human SEIPIN binds anionic phospholipids. *Dev Cell.* 47:248–56.e4. <https://doi.org/10.1016/j.devcel.2018.09.010> PMID: 30293840
32. Sui X, Arlt H, Kelly B, Zong L, Frank D, Debora M, et al. (2018) Cryo-electron microscopy structure of the lipid droplet-formation protein seipin. *J Cell Biol.* 217:4080–91. <https://doi.org/10.1083/jcb.201809067> PMID: 30327422
33. Pagac M, Cooper DE, Qi Y, Lukmantara IE, Mak HY, Wu Z, et al. (2016) SEIPIN regulates lipid droplet expansion and adipocyte development by modulating the activity of glycerol-3-phosphate acyltransferase. *Cell Rep.* 17:1546–59. <https://doi.org/10.1016/j.celrep.2016.10.037> PMID: 27806294
34. Salo VT, Belevich I, Li S, Karhinen L, Vihinen H, Vigouroux C, et al. (2016) Seipin regulates ER–lipid droplet contacts and cargo delivery. *EMBO J.* 24:2699–716. <https://doi.org/10.15252/embj.201695170> PMID: 27879284
35. Salo V, Li S, Vihinen H, Hölttä-Vuori M, Szkalisity A, Horvath P, et al. (2019) Seipin facilitates triglyceride flow to lipid droplet and counteracts droplet ripening via ER contact. *Dev Cell.* 50:478–93.e9. <https://doi.org/10.1016/j.devcel.2019.05.016> PMID: 31178403
36. Grippa A, Buxó L, Mora G, Funaya C, Idrissi F-Z, Mancuso F, et al. (2015) The seipin complex Fld1/Ldb16 stabilizes ER-lipid droplet contact sites. *J Cell Biol.* 211:829–44. <https://doi.org/10.1083/jcb.201502070> PMID: 26572621
37. Wang S, Idrissi FZ, Hermansson M, Grippa A, Ejsing CS, Carvalho P (2018) Seipin and the membrane-shaping protein Pex30 cooperate in organelle budding from the endoplasmic reticulum. *Nat Commun.* 9:2939. <https://doi.org/10.1038/s41467-018-05278-2> PMID: 30054465
38. Cao Z, Hao Y, Lee YY, Wang P, Li X, Xie K, et al. (2019) Dietary fatty acids promote lipid droplet diversity through seipin enrichment in an ER subdomain. *Nat Commun.* 10:2902. <https://doi.org/10.1038/s41467-019-10835-4> PMID: 31263173
39. Cartwright BR, Binns DD, Hilton CL, Han S, Gao Q, Goodman JM (2015) Seipin performs dissectible functions in promoting lipid droplet biogenesis and regulating droplet morphology. *Mol Biol Cell.* 26:726–39. <https://doi.org/10.1091/mbc.E14-08-1303> PMID: 25540432
40. Wang H, Becuwe M, Housden BE, Chitraju C, Porras AJ, Graham MM, et al. (2016) Seipin is required for converting nascent to mature lipid droplets. *Elife.* 5:133–50. <https://doi.org/10.7554/eLife.16582> PMID: 27564575
41. Castro IG, Eisenberg-Bord M, Persiani E, Rochford JJ, Schuldiner M, Bohnert M (2019) Promethin is a conserved seipin partner protein. *Cells.* 8:268. <https://doi.org/10.3390/cells8030268> PMID: 30901948

42. Eisenberg-Bord M, Mari M, Weill U, Rosenfeld-Gur E, Moldavski O, Castro IG, et al. (2018) Identification of seipin-linked factors that act as determinants of a lipid droplet subpopulation. *J Cell Biol.* 217:269–82. <https://doi.org/10.1083/jcb.201704122> PMID: 29187527
43. Teixeira V, Johnsen L, Martínez-Montañés F, Grippa A, Buxó L, Idrissi FZ, et al. (2018) Regulation of lipid droplets by metabolically controlled Ldo isoforms. *J Cell Biol.* 217:127–38. <https://doi.org/10.1083/jcb.201704115> PMID: 29187528
44. Chung J, Wu X, Lambert TJ, Lai ZW, Walther TC, Farese RV (2019) LDAF1 and seipin form a lipid droplet assembly complex. *Dev Cell.* 51:551–63.e7. <https://doi.org/10.1016/j.devcel.2019.10.006> PMID: 31708432
45. Hamilton JA, Miller KW, Small DM (1983) Solubilization of triolein and cholesteryl oleate in egg phosphatidylcholine vesicles. *J Biol Chem.* 258:12821–6. PMID: 6685124
46. Kamiyama D, Sekine S, Barsi-Rhyne B, Hu J, Chen B, Gilbert LA, et al. (2016) Versatile protein tagging in cells with split fluorescent protein. *Nat Commun.* 7:11046. <https://doi.org/10.1038/ncomms11046> PMID: 26988139
47. Li S, Prasanna X, Salo VT, Vattulainen I, Ikonen E (2019) An efficient auxin-inducible degron system with low basal degradation in human cells. *Nat Methods.* 16:866–9. <https://doi.org/10.1038/s41592-019-0512-x> PMID: 31451765
48. Nishimura K, Fukagawa T, Takisawa H, Kakimoto T, Kanemaki M (2009) An auxin-based degron system for the rapid depletion of proteins in nonplant cells. *Nat Methods.* 6:917–22. <https://doi.org/10.1038/nmeth.1401> PMID: 19915560
49. Spandl J, White DJ, Peychl J, Thiele C (2009) Live cell multicolor imaging of lipid droplets with a new dye, LD540. *Traffic.* 10:1579–84. <https://doi.org/10.1111/j.1600-0854.2009.00980.x> PMID: 19765264
50. Hölttä-Vuori M, Salo VT, Ohsaki Y, Suster ML, Ikonen E (2013) Alleviation of seipinopathy-related ER stress by triglyceride storage. *Hum Mol Genet.* 22:1157–66. <https://doi.org/10.1093/hmg/ddt523> PMID: 23250914
51. Sommer C, Straehle C, Ullrich K, Hamprecht FA (2011) Ilastik: interactive learning and segmentation toolkit. In: 2011 8th IEEE International Symposium on Biomedical Imaging: from nano to macro. New York: Institute of Electrical and Electronics Engineers. pp. 230–3.
52. Berg S, Kutra D, Kroeger T, Straehle CN, Kausler BX, Haubold C, et al. (2019) Ilastik: interactive machine learning for (bio)image analysis. *Nat Methods.* 16:1226–32. <https://doi.org/10.1038/s41592-019-0582-9> PMID: 31570887
53. Carpenter AE, Jones TR, Lamprecht MR, Clarke C, Han Kan I, Friman O, et al. (2006) CellProfiler: image analysis software for identifying and quantifying cell phenotypes. *Genome Biol.* 7:100–10. <https://doi.org/10.1186/gb-2006-7-10-r100> PMID: 17076895
54. Pfisterer SG, Gateva G, Horvath P, Pirhonen J, Salo VT, Karhinen L, et al. (2017) Role for formin-like 1-dependent acto-myosin assembly in lipid droplet dynamics and lipid storage. *Nat Commun.* 8:14858. <https://doi.org/10.1038/ncomms14858> PMID: 28361956
55. Schindelin J, Arganda-Carreras I, Frise E, Kaynig V, Longair M, Pietzsch T, et al. (2012) Fiji: an open-source platform for biological-image analysis. *Nat Methods.* 9:676–82. <https://doi.org/10.1038/nmeth.2019> PMID: 22743772
56. Seemann J, Jokitalo EJ, Warren G (2000) The role of the tethering proteins p115 and GM130 in transport through the Golgi apparatus in vivo. *Mol Biol Cell.* 11:635–45. <https://doi.org/10.1091/mbc.11.2.635> PMID: 10679020
57. McLean I, Nakane P (1974) Periodate-lysine-paraformaldehyde fixative a new fixative for immunoelectron microscopy. *J Histochem Cytochem.* 22:1077–83. <https://doi.org/10.1177/22.12.1077> PMID: 4374474
58. Kremer J, Mastronarde D, McIntosh J (1996) Computer visualization of three-dimensional image data using IMOD. *J Struct Biol.* 76:71–6. <https://doi.org/10.1006/jsbi.1996.0013> PMID: 8742726
59. Belevich I, Joensuu M, Kumar D, Vihinen H, Jokitalo E (2016) Microscopy Image Browser: a platform for segmentation and analysis of multidimensional datasets. *PLoS Biol.* 12:e1002340. <https://doi.org/10.1371/journal.pbio.1002340> PMID: 26727152
60. van Meer G, Voelker DR, Feigenson GW (2008) Membrane lipids: where they are and how they behave. *Nat Rev Mol Cell Biol.* 9:112–24. <https://doi.org/10.1038/nrm2330> PMID: 18216768
61. Higgins JA, Dawson RMC (1977) Asymmetry of the phospholipid bilayer of rat liver endoplasmic reticulum. *Biochim Biophys Acta.* 470:342–56. [https://doi.org/10.1016/0005-2736\(77\)90126-2](https://doi.org/10.1016/0005-2736(77)90126-2) PMID: 921959
62. Bollen IC, Higgins JA (1980) Phospholipid asymmetry in rough- and smooth-endoplasmic-reticulum membranes of untreated and phenobarbital-treated rat liver. *Biochem J.* 189:475–80. <https://doi.org/10.1042/bj1890475> PMID: 7213341

63. Devaux PF, Morris R (2004) Transmembrane asymmetry and lateral domains in biological membranes. *Traffic*. 5:241–6. <https://doi.org/10.1111/j.1600-0854.2004.0170.x> PMID: 15030565
64. Ingólfsson HI, Carpenter TS, Bhatia H, Bremer PT, Marrink SJ, Lightstone FC (2017) Computational lipidomics of the neuronal plasma membrane. *Biophys J*. 113:2271–80. <https://doi.org/10.1016/j.bpj.2017.10.017> PMID: 29113676
65. Abraham MJ, Murtola T, Schulz R, Páll S, Smith JC, Hess B, et al. (2015) GROMACS: high performance molecular simulations through multi-level parallelism from laptops to supercomputers. *SoftwareX*. 1–2:19–25.
66. Huang J, Mackerell AD (2013) CHARMM36 all-atom additive protein force field: validation based on comparison to NMR data. *J Comput Chem*. 34:2135–45. <https://doi.org/10.1002/jcc.23354> PMID: 23832629
67. Huang J, Rauscher S, Nawrocki G, Ran T, Feig M, De Groot BL, et al. (2016) CHARMM36m: an improved force field for folded and intrinsically disordered proteins. *Nat Methods*. 14:71–3. <https://doi.org/10.1038/nmeth.4067> PMID: 27819658
68. Klauda JB, Venable RM, Freites JA, O'Connor JW, Tobias DJ, Mondragon-Ramirez C, et al. (2010) Update of the CHARMM all-atom additive force field for lipids: validation on six lipid types. *J Phys Chem B*. 114:7830–43. <https://doi.org/10.1021/jp101759q> PMID: 20496934
69. Guvench O, Mallajosyula SS, Raman EP, Hatcher E, Vanommeslaeghe K, Foster TJ, et al. (2011) CHARMM additive all-atom force field for carbohydrate derivatives and its utility in polysaccharide and carbohydrate-protein modeling. *J Chem Theory Comput*. 7:3162–80. <https://doi.org/10.1021/ct200328p> PMID: 22125473
70. Evans DJ, Holian BL (1985) The Nose–Hoover thermostat. *J Chem Phys*. 83:4069.
71. Parrinello M, Rahman A (1981) Polymorphic transitions in single crystals: a new molecular dynamics method. *J Appl Phys*. 52:7182–90.
72. Marrink SJ, De Vries AH, Mark AE (2004) Coarse grained model for semiquantitative lipid simulations. *J Phys Chem B*. 108:750–60.
73. Darden T, York D, Pedersen L (1993) Particle mesh Ewald: an N-log(N) method for Ewald sums in large systems. *J Chem Phys*. 98:10089–92.
74. De Jong DH, Singh G, Bennett WFD, Arnarez C, Wassenaar TA, Schäfer LV, et al. (2013) Improved parameters for the martini coarse-grained protein force field. *J Chem Theory Comput*. 9:687–97. <https://doi.org/10.1021/ct300646g> PMID: 26589065
75. Monticelli L, Kandasamy SK, Periole X, Larson RG, Tieleman DP, Marrink SJ (2008) The MARTINI coarse-grained force field: Extension to proteins. *J Chem Theory Comput*. 4:819–34. <https://doi.org/10.1021/ct700324x> PMID: 26621095
76. Bussi G, Donadio D, Parrinello M (2007) Canonical sampling through velocity rescaling. *J Chem Phys*. 126:014101. <https://doi.org/10.1063/1.2408420> PMID: 17212484
77. Hanson MA, Cherezov V, Griffith MT, Roth CB, Jaakola VP, Chien EYT, et al. (2008) A specific cholesterol binding site is established by the 2.8 Å structure of the human β_2 -adrenergic receptor. *Structure*. 16:897–905. <https://doi.org/10.1016/j.str.2008.05.001> PMID: 18547522
78. Schmidt HR, Zheng S, Gurpinar E, Koehl A, Manglik A, Kruse AC (2016) Crystal structure of the human σ_1 receptor. *Nature*. 532:527–30. <https://doi.org/10.1038/nature17391> PMID: 27042935
79. Gapsys V, De Groot BL, Briones R (2013) Computational analysis of local membrane properties. *J Comput Aided Mol Des*. 27:845–58. <https://doi.org/10.1007/s10822-013-9684-0> PMID: 24150904
80. Humphrey W, Dalke A, Schulten K (1996) VMD: Visual Molecular Dynamics. *J Mol Graph*. 14:33–8. [https://doi.org/10.1016/0263-7855\(96\)00018-5](https://doi.org/10.1016/0263-7855(96)00018-5) PMID: 8744570
81. Vuorela T, Catta A, Niemelä PS, Hall A, Hyvönen MT, Marrink SJ, et al. (2010) Role of lipids in spheroidal high density lipoproteins. *PLoS Comput Biol*. 6:e1000964. <https://doi.org/10.1371/journal.pcbi.1000964> PMID: 21060857